

Extending the Radial Acceleration Relation using Weak Gravitational Lensing with the Kilo-Degree Survey

Margot M. Brouwer^{1,2*},

¹*Kapteyn Astronomical Institute, University of Groningen, PO Box 800, NL-9700 AV Groningen, the Netherlands.*

²*Institute for Theoretical Physics, University of Amsterdam, Science Park 904, 1098 XH Amsterdam, The Netherlands.*

Accepted XXX. Received YYY; in original form ZZZ

ABSTRACT

TBW

Key words: gravitational lensing; weak – Surveys – methods: statistical – galaxies: haloes – cosmology: dark matter, theory – gravitation.

* E-mail: brouwer@astro.rug.nl

1 INTRODUCTION

It has been known for several decades that the outer regions of galaxies rotate faster than would be expected from Newtonian dynamics based on their luminous, or ‘baryonic’, mass. This was first discovered by [Rubin \(1983\)](#) through measuring galactic rotation curves of optical disks, and by [Bosma \(1981\)](#) through measuring hydrogen profiles at radii beyond the disk. The excess gravity implied by these measurements has been generally attributed to an unknown and invisible substance named Dark Matter (DM), a term coined more than forty years prior by [Zwicky \(1937\)](#) when he discovered the so-called ‘missing mass problem’ through the dynamics of galaxies in clusters.

Following more recent observations using Weak gravitational Lensing (WL, [Hoekstra et al. 2004](#); [von der Linden et al. 2014](#); [Mandelbaum 2015](#)), Baryon Acoustic Oscillations (BAO’s, [Eisenstein et al. 2005](#); [Blake et al. 2011](#)) and the Cosmic Microwave background (CMB, [Spergel et al. 2003](#); [Planck XVI 2014](#)), Cold Dark Matter¹ (CDM) became a key ingredient of the current standard model of cosmology: the Λ CDM model. In this paradigm, CDM accounts for $\Omega_{\text{CDM}} = 0.266$ of the critical density in the Universe, while baryonic matter only accounts for $\Omega_{\text{CDM}} = 0.049$ ([Planck VI 2018](#)). The cosmological constant Λ , which is necessary to explain the accelerated expansion of the Universe and is usually associated with Dark Energy (DE), accounts for $\Omega_{\Lambda} = 0.685$.

Although the Λ CDM model successfully describes the behaviour of DM on a wide range of scales, no conclusive evidence for the existence of DM particles has been found so far (despite years of enormous effort; for an overview, see [Bertone et al. 2005](#); [Bertone & Tait 2018](#)). This still leaves some room for alternative theories of gravity, such as Modified Newtonian Dynamics (MOND, [Milgrom 1983](#)) and the more recent theory of Emergent Gravity (EG, [Verlinde 2016](#)). In these theories particle DM does not exist, and all gravity is due to the baryonic matter (or, in the case of EG, the interaction between baryons and the entropy associated with DE). Hence, one of the main properties of these theories is that the mass discrepancy in galaxies correlates strongly with their baryonic mass distribution.

Such a correlation has indeed been widely observed. First astronomers discovered the Tully-Fisher relation (TFR, [Tully & Fisher 1977](#)) between the luminosity of a spiral galaxy and its asymptotic rotation velocity ([Pierce & Tully 1988](#); [Bernstein et al. 1994](#)). Since this corresponds to a relation between the baryonic and the total galaxy mass, this has later been named the ‘baryonic’ TFR (BTFR, [McGaugh et al. 2000](#); [McGaugh 2012](#)). As the radial resolution of observations increased, astronomers found a strong correlation between the observed rotation velocity $v_{\text{obs}}(r)$ as a function of galaxy radius r , and the enclosed luminous mass $M_b(< r)$ ([Sanders 1986, 1996](#); [McGaugh 2004](#); [Sanders & Noordermeer 2007](#); [Wu & Kroupa 2015](#)). Since $M_b(< r)$ corresponds to the *expected* gravitational acceleration $g_b(r)$ from baryonic matter, and the observed gravitational acceleration can be calculated through $g_{\text{obs}}(r) = v_{\text{obs}}^2(r)/r$, this

relation has been named the Radial Acceleration Relation (RAR)².

Particularly, the latest results from [McGaugh et al. \(2016\)](#) (hereafter M16) have measured the RAR relation with unprecedented accuracy, using the Spitzer Photometry and Accurate Rotation Curves (SPARC, [Lelli et al. 2016](#)) data of 153 late-type galaxies. Their results showed a tight correlation between g_{obs} and g_{bar} , which they could fit using a simple double power law (Eq. 4 in M16) depending only on g_{bar} and one free parameter: the acceleration scale g_{\dagger} where Newtonian gravity appears to break down. This sparked the interest of scientists working on alternative theories of gravity, but also of those in favor of a statistical explanation of the RAR within the Λ CDM framework ([Keller & Wadsley 2017](#); [Desmond 2017](#); [Ludlow et al. 2017](#)).

The latter possibility was quantified by [Navarro et al. \(2017\)](#) (hereafter N17) who used a range of simplifying assumptions based on galaxy observations and DM simulations, in order to create an analytical galaxy+halo model. The goal of their model was to reconstruct the RAR in galaxies, in particular the value of a_0 : the acceleration scale where the relation transitions from the baryon-dominated to the DM-dominated regime (which is equivalent to g_{\dagger}), and a_{min} : the minimum acceleration probed by galaxy disks. Based on their results, they claimed that the RAR can be explained within the Λ CDM framework, at the accelerations probed by galaxy rotation curves (i.e. $g_{\text{obs}} > a_{\text{min}}$). However, since their model relies on the fact that luminous kinematic tracers in galaxies only probe a limited radial range, N17 predicted that extending observations to radii beyond the disk (which correspond to lower gravitational accelerations) would lead to systematic deviations from the simple relation posed by M16.

The goal of this work is to extend observations of the RAR to lower accelerations, which are not measurable using galaxy rotation curves. To this end we use gravitational lensing: the perturbation of light inside a gravitational potential as described by General Relativity (GR). In particular, we use the method of Galaxy-Galaxy Lensing (GGL): the statistical measurement of the coherent image distortion (shear) of a field of background galaxies by the gravitational potential of a sample of foreground galaxies (for examples, see e.g. [Fischer et al. 2000](#); [Hoekstra et al. 2004](#); [Mandelbaum et al. 2006](#); [van Uitert et al. 2016](#)). Using GGL we can measure the average (apparent) density distribution of galaxies up to a radius of 3 Mpc, roughly a 100 times larger than the radius of the luminous disk (~ 30 kpc), corresponding to a value of g_{bar} that is 3 orders of magnitude lower than those measurable with galaxy rotation curves.

First, we measure the baryonic and total density profiles of our galaxies through their luminosities and GGL profiles. These measurements will be performed using photometric data from Sloan Digital Sky Survey ([Abazajian et al. 2009](#), SDSS,) and the VISTA Kilo-Degree Infrared Galaxy survey ([Edge et al. 2013](#), VIKING), and WL data from the Kilo-

¹ DM particles that moved at non-relativistic speeds at the time of recombination, as favoured by measurements of the CMB ([Planck XVI 2014](#)) and the Lyman- α forest ([Viel et al. 2013](#)).

² Another well-established name for this same relation is the Mass-Discrepancy Acceleration Relation (MDAR), which refers to the correspondence between the observed baryonic/total mass and the inferred mass discrepancy commonly attributed to DM. Throughout this work we use the term RAR for brevity.

Degree Survey (KiDS; [de Jong et al. 2013](#)). We then translate these measurements into the baryonic and observed radial accelerations, g_{bar} and g_{obs} . Finally, we compare the resulting RAR to predictions from different modified gravity theories (MOND and EG) and Λ CDM.

The Λ CDM predictions will not only be provided by the N17 analytical model, but also by two mock galaxy catalogues based on two different DM simulations. One is the Marenostrum Institut de Ciències de l’Espai (MICE) Galaxy and Halo Light-cone catalogue ([Carretero et al. 2015](#); [Hoffmann et al. 2015](#)), which is based on the MICE Grand Challenge lightcone simulation (MICE-GC, [Fosalba et al. 2015a,b](#); [Crocce et al. 2015](#)). The other mock galaxy catalogue is based on a suite of large-volume cosmological hydrodynamical simulations, which is called the Baryons and HALoes of MAssive Systems (BAHAMAS) project ([McCarthy et al. 2017](#)). Our final goal is to distinguish which of the aforementioned predictions best describe the RAR at lower accelerations.

Having almost a million foreground galaxies at our disposal, we are able to select specific galaxy samples designed to optimally test these predictions. Particularly, we note that most models (MOND, EG, and the N17 analytical DM model) focus on the description of individual, isolated galaxies. In order to test them, therefore, we select a sample of galaxies whose lensing profiles are not affected by their neighbours within the radius of our measurement. In contrast, the predictions from the MICE and BAHAMAS simulations can be tested for both isolated and non-isolated galaxy samples.

Furthermore, we note that all models give a specific prediction regarding the dependence of the RAR on baryonic galaxy mass. According to the MOND and EG theories, the relation between g_{bar} and g_{obs} should remain intact in the regime beyond the disk, independent of the disk mass. Within the Λ CDM paradigm, however, all predictions (analytical and simulated) are based on a ‘stellar-to-halo-mass relation’ which is not constant as a function of baryonic galaxy mass. By splitting our foreground galaxies into bins of increasing stellar mass, we are able to better distinguish the predictions of these different models.

Our paper is structured as follows: In Sect. 2 we introduce our main datasets: both the KiDS and GAMA galaxy surveys which are used to perform the GGL measurements, and the MICE and BAHAMAS simulations & mock galaxy catalogues to which we compare our results. Sect. 3 describes our analysis of these (mock) datasets as we select our isolated foreground galaxy sample, perform the GGL measurements, and translate the results into the RAR. Sect. 5 contains a description of the theoretical predictions to which we compare our observations: MOND, EG and the N17 analytical DM model. In Sect. 6 we present the resulting RAR measurements and model comparison. Sect. 7 contains the discussion and conclusion.

Throughout this work we adopt the WMAP 9-year ([Hinshaw et al. 2013](#)) cosmological parameters: $\Omega_{\text{m}} = 0.2793$, $\sigma_8 = 0.821$, $\Omega_{\Lambda} = 0.7207$, and $H_0 = 70 \text{ km s}^{-1} \text{ Mpc}^{-1}$, which were used as the basis of the BAHAMAS simulation. The cosmological parameters used in creating the MICE-GC simulations are: $\Omega_{\text{m}} = 0.25$, $\sigma_8 = 0.8$, $\Omega_{\Lambda} = 0.75$, and $H_0 = 70 \text{ km s}^{-1} \text{ Mpc}^{-1}$. Through-

out the paper we use the reduced Hubble constant $h_{70} \equiv H_0 / (70 \text{ km s}^{-1} \text{ Mpc}^{-1})$.

2 DATA

2.1 KiDS source galaxies

We use Galaxy-Galaxy Lensing (GGL) to measure the gravitational potential around a sample of foreground galaxies (lenses), by measuring the image distortion (shear) of a field of background galaxies (sources). These sources are observed using OmegaCAM ([Kuijken 2011](#)): a 268-million pixel CCD mosaic camera mounted on the VLT Survey Telescope ([Cappacioli & Schipani 2011](#)). Over the past seven years these instruments have performed KiDS, a photometric survey in the *ugri* bands, which is especially designed to perform WL measurements ([de Jong et al. 2013](#)).

GGL studies with KiDS have hitherto been performed in combination with the spectroscopic GAMA survey (see Sect. 2.2 below). Already since the previous data release (KiDS-DR3, [de Jong et al. 2017](#)) the KiDS survey completely covers the 286 deg^2 GAMA area. Although the final survey will span 1350 deg^2 on the sky, the current state-of-the-art is the 4th Data Release (KiDS-DR4, [Kuijken et al. 2019](#)) containing observations from 1006 square-degree survey tiles. The measurement of the source shapes and photometric redshifts are performed in similar fashion to [de Jong et al. \(2017\)](#). Changes and improvements to these methods are described in [Kuijken et al. \(2019\)](#).

The measurements of the galaxy shapes are based on the *r*-band data, since this filter was used during the darkest time (moon distance $> 90 \text{ deg}$) and with the best atmospheric seeing conditions ($< 0.8 \text{ arcsec}$). The *r*-band observations are co-added using the THELI pipeline ([Erben et al. 2013](#)), which is improved through the addition of an illumination correction. From these images the galaxy positions are detected through the SExtractor algorithm ([Bertin & Arnouts 1996](#)). After detection, the shapes of the galaxies are measured using the *lensfit* pipeline ([Miller et al. 2007, 2013](#)), which includes a self-calibration algorithm based on [Fenech Conti et al. \(2017\)](#). Each shape is accompanied by a *lensfit* weight w_s , which gives an estimate of the precision of the ellipticity measurement.

For the purpose of creating the photometric redshift and stellar mass estimates, eight additional bands are observed. The *u*, *g* and *i* bands are observed by KiDS, while the VISTA Kilo-degree Infrared Galaxy survey (VIKING, [Edge et al. 2013](#)) performed on the VISTA telescope adds the *ZYJHK_s* bands. All bands are reduced and co-added using the Astrowise (AW) pipeline ([McFarland et al. 2013](#)). The galaxy colours, which form the basis of the photometric redshift measurements, are measured from these images using the Gaussian Aperture and PSF pipeline (GAAP [Kuijken 2008](#); [Kuijken et al. 2015](#)).

The addition of the lower frequency VISTA data allows us to extend the redshift estimates out to $0.1 < z_{\text{B}} < 1.2$ (instead of $0.1 < z_{\text{B}} < 0.9$ in KiDS-DR3), where z_{B} is the best-fit photometric redshift of the sources ([Benítez 2000](#); [Hildebrandt et al. 2012](#)). However, when performing our lensing measurements (see 3.1) we use the total redshift probability distribution function (PDF) n_z of the full source population.

This n_z is calculated using the direct calibration method (DIR, [Hildebrandt et al. 2017](#)), and circumvents the inherent bias related to photometric redshift estimates of individual sources.

2.2 GAMA foreground galaxies

Although the final RAR measurements will be performed using exclusively the KiDS-DR4 data, the set of foreground galaxies observed by the spectroscopic GAMA survey ([Driver et al. 2011](#)) function both as a model and validation sample for the KiDS foreground galaxies. The survey was performed by the Anglo-Australian Telescope with the AAOmega spectrograph, and targeted more than 180 000 galaxies that were selected from SDSS. For this study we use the GAMA II data release ([Liske et al. 2015](#)) consisting of three equatorial regions (G09, G12 and G15). These regions span a total area of $\sim 180 \text{ deg}^2$ on the sky, completely overlapping with KiDS.

GAMA has a redshift range of $0 < z < 0.5$, with a mean redshift of $\bar{z} = 0.22$. The survey has a redshift completeness of 98.5% down to Petrosian r-band magnitude $m_{r,\text{Petro}} = 19.8 \text{ mag}$. We limit our GAMA foreground sample to galaxies with the recommended redshift quality: $n_Q \geq 3$. The GAMA spectroscopic redshifts are used to train the photometric machine-learning (ML) redshifts of our larger sample of KiDS foreground galaxies (see Sect. 2.3).

Despite being a smaller survey, GAMA's accurate redshifts are highly advantageous when measuring the ESD profiles of galaxies (see Sect. 3.1). Also, in combination with its high redshift completeness, GAMA allows for a better application of the isolation criterion. We therefore check that the results from the KiDS-only measurements are consistent with those from KiDS-GAMA at all times.

To measure the RAR with KiDS-GAMA, we need individual stellar masses M_* for each GAMA galaxy. These are measured from their *ugrizZYJHK* spectral energy distributions³ measured by SDSS and the VISTA Kilo-Degree Infrared Galaxy survey (VIKING, [Edge et al. 2013](#)), by fitting them with [Bruzual & Charlot \(2003\)](#) stellar population synthesis models. Following the procedure described by [Taylor et al. \(2011\)](#), we account for flux falling outside the automatically selected aperture using the 'flux-scale' correction.

2.3 KiDS foreground selection

Still need to know:

- Maciek's GL-KiDS selection criteria for K1000.
- Angus' stellar mass method for K1000.

As our lenses, we select a 'GAMA-like' (GL) sample of foreground galaxies from $\sim 1000 \text{ deg}^2$ of KiDS-DR4 data ([Kuijken et al. 2019](#)). To mimic the magnitude limit of GAMA ($m_{r,\text{Petro}} < 19.8 \text{ mag}$), we apply a similar cut to the (much deeper) KiDS survey. Because the KiDS catalogue does not contain Petrosian magnitudes, we use the calibrated Kron-like elliptical aperture *r*-band magnitudes

'MAG_AUTO'⁴ from SExtractor, which have a very similar distribution. Through matching the KiDS and GAMA galaxies and seeking the best trade-off between completeness and purity, we decide to limit our GL-KIDS sample to $m_{r,\text{auto}} < 20.0$. In addition, we limit the redshifts of the GL-KiDS galaxies to the maximum GAMA redshift ($z_G < 0.5$).

To remove any stellar contamination we apply three independent cuts, based on galaxy morphology, the 9-band photometry and the SExtractor star/galaxy classifier respectively.⁵ We also remove galaxies that are affected by read-out and diffraction spikes, saturation cores, bad pixels, or by primary, secondary or tertiary haloes of bright stars.⁶ In addition, we apply the recommended '9-band no AW-r-band mask', which is also used to create the KiDS-DR4 shear catalogues.⁷ For more information on these masks, we refer the reader to App. A of [Kuijken et al. \(2019\)](#). Our final sample GL-KiDS lenses consists of 1.2×10^6 (9.85×10^5) galaxies with a mean redshift of $\bar{z}_{\text{ANN}} = 0.24$, which slightly higher than that of GAMA ($\bar{z} = 0.22$).

To apply the aforementioned redshift limit, and more importantly to use the GL-KiDS sample as lenses to measure g_{obs} , we need accurate individual redshifts for all galaxies in our sample. These photometric redshifts z_{ANN} are derived from the KiDS *ugri* photometry (the full 9-band KiDS+VIKING photometry) (see Sect. 2.1), by training on the spectroscopic GAMA redshifts (see Sect. 2.2) using the ANNz2 machine learning method ([Sadeh et al. 2016](#); [de Jong et al. 2017](#); [Bilicki et al. 2017](#)). Objects that are not detected in all 4 (9) bands are removed from the sample. When comparing z_{ANN} and z_G redshifts measured for the same galaxies, we find that the mean ANNz2 redshift error is $(z_{\text{ANN}} - z_G)/(1 + z_G) = 8.35 \times 10^{-4}$ (TBD for 9-band M_*) with a standard deviation $\sigma_z = 0.026$ (0.022). This corresponds to a redshift-dependent deviation of $\sigma_z/(1 + z) = 0.021$ (0.018), based on our value of \bar{z}_{ANN} .

In order to measure the expected baryonic acceleration g_{bar} , we compute stellar masses $M_{*,\text{ANN}}$ based on these ANNz2 redshifts and the 9-band GAAP photometry. This is achieved using the LEPHARE algorithm ([Arnouts et al. 1999](#); [Ilbert et al. 2006](#)), which performs fits of stellar synthesis models on the stellar component of the galaxies' Spectral Energy Distribution (SED). LePhare provides both the best-fit M_* value 'MASS_BEST' of the galaxy template PDF, and the 68% confidence level upper and lower limits. Because the GAAP photometry only measures the galaxy magnitude within a specific aperture size, this stellar mass is corrected using a 'fluxscale' parameter, such that: $M_* = \text{LBEST} + (\text{MAG_GAAP}_r - \text{MAG_AUTO_CALIB}) / 2.5$.

When comparing $M_{*,\text{ANN}}$ with the GAMA stellar masses $M_{*,G}$ of matched galaxies, we find that its distribution is very similar, with a standard deviation of 0.25 dex. Nevertheless, we find a systematic offset of $\log(M_{*,\text{ANN}}) -$

⁴ This will be updated to 'MAG_AUTO_CALIB' for the updated GL-KiDS catalogue.

⁵ Our star-galaxy separation corresponds to applying the following flags: SG2DPHOT=0, SG_FLAG=1, CLASS_STAR<0.5.

⁶ This masking corresponds to applying all MASK values (1, 2, 4, 8, 16, 32 and 64) described in App. A.1.1 of [Kuijken et al. \(2019\)](#), through applying the flag: IMAFLAGS_ISO=0.

⁷ This masking corresponds to the 9-band MASK bit values 2 to 11, 13 and 14, described in App. A.2 of [Kuijken et al. \(2019\)](#).

³ The spectral energy distributions are constrained to the rest frame wavelength range 3000 – 110000 Å.

$\log(M_{*,G}) = -0.11$ dex, which is caused by the different stellar mass estimation methods used on the two surveys. This is a problem inherent to the variety of possible stellar population synthesis models, based on different Initial Mass Functions (IMFs). In general, it has thus far been impossible to constrain stellar masses within a systematic uncertainty of $\Delta M_* \sim 0.1$ dex (reference Angus ...). In this work we therefore normalize the $M_{*,ANN}$ values of our GL-KiDS sample to the mean $M_{*,G}$ of GAMA, while indicating throughout our results the range of possible bias due to a $\Delta M_* = 0.1$ dex shift in M_* . We estimate the effect of this bias by computing the RAR with $\log(M_*) \pm \Delta M_*$ as upper/lower limits.

2.4 MICE mock galaxies

In order to compare our observations to predictions from Λ CDM, we adopt two different DM simulations. One of these is the MICE-GC N -body simulation, which contains $\sim 7 \times 10^{10}$ DM particles in a $(3072 h_{70}^{-1} \text{Mpc})^3$ comoving volume (Fosalba et al. 2015b). From this simulation the MICE collaboration constructed a $\sim 5000 \text{ deg}^2$ lightcone with a maximum redshift of $z = 1.4$. The DM halos in this lightcone are identified using a Friend-of-Friend (FOF) algorithm on the particles. These DM halos were populated with galaxies using a hybrid Halo Occupation Distribution (HOD) and Halo Abundance Matching (HAM) prescription (Carretero et al. 2015; Crocce et al. 2015).

In the MICECATv2.0 catalogue⁸ which we use in this work, every galaxy has sky coordinates, redshifts, comoving distances, apparent magnitudes and absolute magnitudes assigned to them. We use the SDSS apparent r -band magnitudes m_r , as these most closely match those from KiDS (see Brouwer et al. 2018). We can therefore limit the MICE galaxies to the same apparent magnitude as the GL-KiDS sample: $m_r < 20$ mag, in order to create a GL-MICE foreground galaxy sample. We also use the same redshift limit: $z < 0.5$, resulting in a mean GL-MICE redshift equal to the mean GAMA redshift: $\bar{z} = 0.22$. The absolute magnitudes of the mock galaxies go down to $M_r - 5 \log_{10}(h) < -14$ mag, which corresponds to the faintest GAMA and GL-KiDS galaxies. New to this version, is that each galaxy is also assigned a stellar mass M_* needed to compute the RAR (see Sect. 4). These stellar masses are determined from the galaxy luminosities L using Bell & de Jong (2001) M/L ratios.

In addition, each galaxy has a pair of lensing shear values associated with it (γ_1 and γ_2 , with respect to the Cartesian coordinate system). These shear values were calculated from healpix weak lensing maps that were constructed using the ‘onion shell method’ (Fosalba et al. 2008, 2015a). The lensing map of MICECATv2.0 has an improved resolution of 0.43 arcmin, which is almost twice smaller than that of MICECATv1.0 (0.85 arcmin). At the mean GL-MICE redshift this resolution corresponds to a projected distance of $R \sim 0.1 h^{-1} \text{Mpc}$, and we will indicate this radius wherever MICE results are shown in this work. At scales larger than this limit, the MICE shears allow us approximate the lensing analysis we perform on our KiDS data (as described in

Section 3.1) using the MICE simulation. To create a sample of MICE background galaxies for the lensing analysis, we apply limits on the MICE mock galaxies’ redshifts and apparent magnitudes which are analogous to those applied to the KiDS source sample: $0.1 < z < 0.9$, $m_r > 20$ (see Hildebrandt et al. 2017 and Sect. 2.1; note that uncertainties in the KiDS z_B are not accounted for in this selection). We also apply an absolute magnitude cut of $M_r > 19.3$ mag, in order to resemble the KiDS source redshift distribution more closely.

The MICE-GC mock catalogue also features very accurate clustering. At lower redshifts ($z < 0.25$) the clustering of the mock galaxies as a function of luminosity is constructed to reproduce the SDSS clustering observations (Zehavi et al. 2011), while at higher redshifts ($0.45 < z < 1.1$) it was validated against the Cosmic Evolution Survey (COSMOS, Ilbert et al. 2009). This makes MICE especially suitable to reproduce the RAR at larger scales ($> 1 h^{-1} \text{Mpc}$) where neighbouring galaxies start to affect the lensing signal, and to test our criteria considering the galaxy isolation (see Section 3.2).

2.5 BAHAMAS mock galaxies

Written by Kyle.

3 DATA ANALYSIS

3.1 Lensing measurement

The measurement of the projected mass density that we use to estimate the gravitational acceleration around galaxies (see Sect. 4), is obtained through the WL method (for a general introduction, see Bartelmann & Schneider 2001; Schneider et al. 2006). More specifically, we use GGL: the measurement of the coherent image distortion of a field of background galaxies (sources) by the gravitational potential of a sample of foreground galaxies (lenses). Because the individual image distortions are very small (only $\sim 1\%$ compared to the galaxy’s unknown original shape), this method can only be performed statistically for a large sample of sources. We average their projected ellipticity component ϵ_t tangential to the direction of the lens galaxy, which is the sum of the intrinsic ellipticity ϵ_{int} and the tangential shear γ_t caused by WL. Assuming no preferential alignment in the intrinsic galaxy shapes ($\langle \epsilon_{\text{int}} \rangle = 0$), the average $\langle \epsilon_t \rangle$ is an estimator of γ_t . By measuring this averaged quantity in circular annuli around the lens centre, we obtain the shear profile $\gamma_t(R)$ as a function of projected radius R .

The lensing shear profile can be related to the physical Excess Surface Density (ESD) profile:

$$\Delta\Sigma(R) = \Sigma_{\text{crit}}\gamma_t(R) = \bar{\Sigma}(<R) - \Sigma(R), \quad (1)$$

which is the surface density $\Sigma(R)$ at projected radius R , subtracted from the average surface density $\bar{\Sigma}(<R)$ within R . The conversion factor between γ_t and $\Delta\Sigma$ is the inverse of the critical surface density, also called the lensing efficiency:

$$\Sigma_{\text{crit}}^{-1} = \frac{4\pi G}{c^2} \int_{z_1}^{\infty} D(z_1) \left(\int_{z_1}^{\infty} \frac{D(z_1, z_s)}{D(z_s)} n(z_s) dz_s \right) p(z_1) dz_1, \quad (2)$$

⁸ The MICECATv2.0 catalogue is available through CosmoHub (<https://cosmohub.pic.es>).

where $D(z_l)$ and $D(z_s)$ are the angular diameter distances to the lens and the source respectively, and $D(z_l, z_s)$ the distance between them. The constant multiplication factor is defined by the speed of light c and Newton's gravitational constant G . For the lens redshifts z_l , we use the ANNz machine-learning redshifts of the KiDS foreground galaxy sample (see Sect. 2.3). We implement the contribution of z_l by integrating over the individual redshift probability distributions $p(z_l)$ of each lens. This $p(z_l)$ is defined by a normal distribution centred at the lens' z_{ANN} redshift, with a standard deviation: $\sigma_z/(1+z) = 0.021$ (0.0018). For the source redshifts z_s we follow the method used in Dvornik et al. (2018), by integrating over the part of the redshift probability distribution $n(z_s)$ where $z_s > z_l$. In addition, sources only contribute their shear to the lensing signal when $z_B + \Delta z > z_l$, i.e. the sum of their best-fit photometric redshift z_B and the redshift buffer $\Delta z = 0.2$ is greater than the lens redshift. Following Brouwer et al. (2017), we measure the ESD profiles between: $0.03 < R < 30 h^{-1} \text{Mpc}$.

To increase the signal-to-noise ratio (S/N) of the lensing signal even further, the ESD profile is averaged (or 'stacked') for large samples of lenses. We define a lensing weight W_{ls} which depends on both the *lensfit* weight w_s and the lensing efficiency $\Sigma_{\text{crit}}^{-1}$:

$$W_{ls} = w_s (\Sigma_{\text{crit},ls}^{-1})^2, \quad (3)$$

and use it to optimally sum the measurements from all lens-source pairs into the average ESD:

$$\Delta\Sigma = \frac{1}{1+\mu} \frac{\sum_{ls} W_{ls} \epsilon_{t,ls} \Sigma_{\text{crit},ls}}{\sum_{ls} W_{ls}}. \quad (4)$$

Here the factor $(1+\mu)$ corrects for the 'multiplicative bias' (Fenech Conti et al. 2017). Extending the method of Dvornik et al. (2017) to the higher KiDS-DR4 redshifts, μ is calculated from the multiplicative bias corrections m of the individual sources:

$$\mu = \frac{\sum_s w_s m_s}{\sum_{ls} w_s}, \quad (5)$$

in 11 linear redshift bins between $0.1 < z_B < 1.2$. The value of this correction is $\mu \approx 0.014$, independent of the projected distance from the lens. After correction, the effects of the multiplicative bias are reduced to $< 1\%$.

We also correct our lensing signal for effects from residual shape correlations due to the (small) PSF anisotropy of the KiDS observations. At the survey edges, it is possible that the averaging of the source shapes is not performed over all azimuthal angles, which can result in systematic effects on the ESD at larger scales ($R > 1 h^{-1} \text{Mpc}$). We correct for this by subtracting the ESD profile measured around random points. From the basic random catalogue created for the KiDS survey, we use a randomly selected sample of ... coordinates, which is ... times the size of our total GL-KiDS sample. These random coordinates mimic the exact footprint of KiDS, including the areas masked by the '9-band no AWR-band' mask which was also applied to the GL-KiDS lenses (see Sect. 2.3). In order to create random redshift values that mimic the true distribution, we create a histogram of the GL-KiDS redshifts divided into 100 linear bins between $0 < z_{\text{ANN}} < 0.5$. In each bin, we create random redshift values equal to the number of real lenses in that bin. We find that the resulting random lensing signal is very small, with a

mean absolute value of only $\sim 3\%$ of the lensing signal of the GL-KiDS galaxies. Because of the large contiguous area of KiDS-DR4, the random ESD profile is consistent with zero at all projected radii R .

The error values on the ESD profile are estimated by the square-root of the diagonal of the analytical covariance matrix, which is described in Sect. 3.4 of Viola et al. (2015). The full covariance matrix is calculated based on the contribution of each individual source to the ESD profile, and incorporates the correlation between sources that contribute to the ESD in multiple bins, both in projected distance R and stellar mass M_* .

The GGL method described above is basically identical to the procedure used by recent KiDS-GGL papers, specifically: Dvornik et al. (2017, 2018) and Brouwer et al. (2017, 2018). For more details on the KiDS-GGL procedure, we recommend reading these recent works. The method that was used in older works (Viola et al. 2015; Sifón et al. 2015; van Uitert et al. 2016; Brouwer et al. 2016) is also very similar, although small changes have occurred in the pipeline with the arrival of new data-releases.

Note that we use the unadulterated GGL method throughout this work, also when testing the MOND and EG theories. We recognize that, by using the basic GGL equations to measure the (apparent) density distributions in these frameworks, we necessarily assume that the laws of GR hold with respect to the deflection of light by a gravitational potential. We therefore motivate in Sect. 5.1 and 5.2 why this assumption holds for the alternative gravity theories we test in this work.

3.2 Isolated galaxy selection

After performing the measurement of the RAR using GGL, our final goal is to compare the results to different analytical models (see Sect. 5) and N-body simulations (see Sect. 2.4 and 2.5) which make specific predictions on the galaxy-halo connection. While the simulations are designed to describe galaxies in their cosmological environment, the analytical models mainly focus on the description of individual galaxies. This means that, in order to test these models, we need to select galaxies that are relatively isolated. Most importantly, their measured ESD profiles should not be significantly affected by neighbouring galaxies, which we will call 'satellites'. We define our isolated lenses such that they not have any satellites with more than a fraction $f_{M_*} \equiv M_{*,\text{sat}}/M_{*,\text{lens}}$ of their stellar mass, within a spherical radius r_{sat} . We choose $f_{M_*} = 0.1$ which corresponds to 10% of the lens stellar mass, and $r_{\text{sat}} = 3 h^{-1} \text{Mpc}$ which is equal to the maximum projected radius of our measurement. In short: $r_{\text{sat}}(f_{M_*} > 0.1) > 3 h^{-1} \text{Mpc}$. We also restrict our lens stellar masses to $\log(M_*) < 11 h^{-2} M_\odot$, since galaxies with higher masses have significantly more satellites (see Sect. 2.2.3 of Brouwer et al. 2017) ... and (hot) gas?...

We validate our isolation criterion using the GL-KiDS data and -MICE datasets. Tests with higher values of r_{sat} do not yield any decrease in the GGL signal at larger ($> 1 h^{-1} \text{Mpc}$) scales, or 2-halo term, which corresponds to the contribution of satellites. This is true both when all lens masses are considered, and when they are restricted to a specific stellar mass ($\log(M_*) = 10.5 \pm 0.1 h^{-2} M_\odot$). Using lenses with this same stellar mass we perform a test where we

reduce the satellite mass fraction to $f_{M_*} = 0$ (corresponding to no visible satellites). This also yields no decrease in the 2-halo term of the ESD profile. When we restrict the *total* stellar mass M_{tot} of all satellites within r_{sat} to $f_{M_{\text{tot}}} < 0.1$ this does not significantly affect the isolated lens sample (i.e. the samples selected with KiDS are $> 99\%$ overlapping), because galaxies with $f_{M_*} \ll 0.1$ are not likely to be observed in a flux-limited survey. Finally, we apply our isolation criterion to the GAMA survey, to compare our selected isolated sample with the ‘isolated centrals’ that were used by Brouwer et al. (2017). In that work we used a more elaborate isolation criterion, which was driven by the Friends-of-Friends (FoF) group finding algorithm of Robotham et al. (2011). We find that the two isolated galaxy samples are more than 80% overlapping.

However, because both the GAMA survey and the GL-KiDS and -MICE samples designed to mimic it are flux-limited, satellites that are fainter than the flux limit are not detected. This can cause lenses that are close to the magnitude limit ($m_{\text{lim}} = 20$ mag) to be falsely identified as isolated. This problem is illustrated in Fig. 1, which shows that the fraction of galaxies assigned to the isolated lens sample increases for higher values of the apparent r -band magnitude m_r . The dashed vertical line represents the magnitude m_{bright} , below which all satellites with a luminosity fraction larger than $f_L \equiv L_{\text{sat}}/L_{\text{lens}} = 0.1$ compared to the lens are still detected. In the case of GL-KiDS:

$$m_{\text{bright}} < m_{\text{lim}} - 2.5 \log_{10}(f_L = 0.1) < 17.5 \text{ mag}. \quad (6)$$

Applying this magnitude cut provides us with an isolated lens sample that is relatively free of false candidates, allowing us to estimate their effect on the ESD profiles. In Fig. 2 we compare the ESD profiles of isolated galaxies with the more reliable ‘bright’ sample. Due to the smaller number of lenses, the ESD errors and scatter of the bright isolated sample are much larger than those of the full isolated sample. Nevertheless, it is clear that their ESD profiles show consistent behaviour at both small and large scales. Compared to the total (non-isolated) galaxy sample their small-scale lensing signal (or 1-halo term, corresponding to the lens itself) is increased, due to the slightly higher masses of the isolated samples. As expected, their large-scale signal (or 2-halo term, corresponding to the contribution of satellites) is decreased. The high level of consistency between the ESD profiles of the regular and bright isolated galaxies, indicates that the effect of false candidates is limited.

Nevertheless, we use the MICE simulations to perform one additional test. We select the isolated sample of GL-MICE lenses using a sample of galaxies that extends to $m_r < 22.5$ mag, such that all satellites with $f_L > 0.1$ can be observed. This paints a similar picture as the bright KiDS sample, i.e.: although the much smaller sample of isolated galaxies selected using the faint satellites greatly increases the scatter, we find no consistent decrease in the lensing signal at $> 1 h^{-1} \text{Mpc}$ scales compared to the original sample of isolated GL-MICE galaxies. While these tests demonstrate the overall robustness of our isolation criterion, we note that this issue is only relevant when comparing our observations to the theoretical models (EG, MOND and N17). When comparing to the N-body simulations (BAHAMAS and MICE), applying the same criterion to both data and

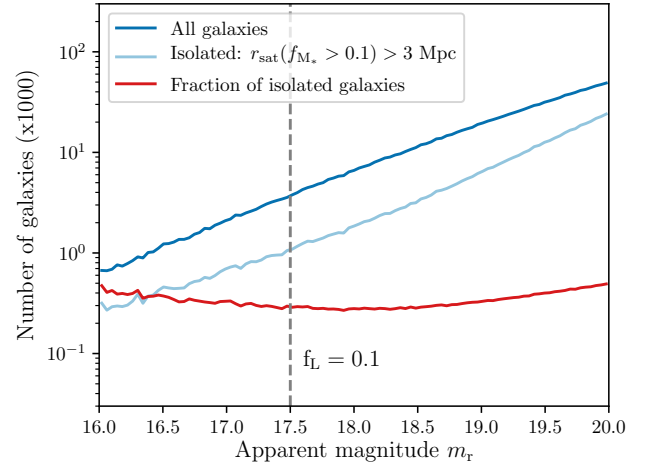


Figure 1. TBW

mocks ensures that any issues with the isolated galaxy selection are mimicked.

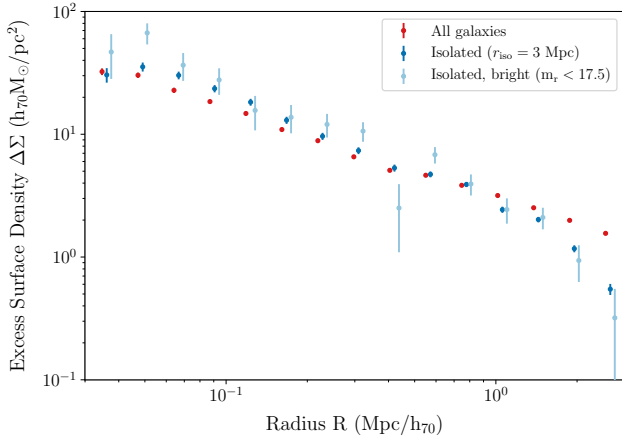
One difference between the isolated galaxy selection of mock galaxies compared to GL-KiDS, is that for the mocks the true redshift values are known, whereas the ANNz photometric redshifts are only known within a certain standard deviation σ_z (see Sect. 2.3). This affects the observed spherical distances r between the galaxies, a key ingredient of the isolation criterion. The redshift uncertainty also affects the GL-KiDS stellar mass estimates, which influences both the isolation criterion (through f_{M_*}) and the application of the stellar mass limit: $\log(M_*) < 11 M_\odot$. We assess the effect of these uncertainties on the isolated galaxy selection by adding a normally distributed random offset with $\sigma_z/(1+z) = 0.021$ (0.018) to the MICE redshifts, and $\sigma_{M_*} = 0.25$ dex (TBD for 9-band M_*) to the stellar masses. Because the random redshift offset decreases the galaxy clustering, it increases the number of galaxies selected by the isolation criterion, adding galaxies which are not truly isolated to the lens sample (as well as excluding some truly isolated galaxies). The ESD profile of the isolated sample selected using this ‘offset’ MICE data is shown in Fig. 3 compared to the ESD for all MICE galaxies (without any isolation criterion) and the isolated galaxies selected using the true MICE data.

4 CONVERSION TO THE RAR

After measuring the lensing profile around a galaxy sample, the next important step is to convert it into the corresponding RAR. We start from the ESD as a function of projected radius ($\Delta\Sigma(R)$) and the measured stellar masses of the lens galaxies (M_*), and aim to arrive at their observed radial acceleration g_{obs} as a function of their expected baryonic radial acceleration g_{bar} . The latter can be calculated using Newton’s law of universal gravitation:

$$g(r) = \frac{G M(< r)}{r^2}. \quad (7)$$

which defines the radial acceleration g in terms of the gravitational constant G and the enclosed mass $M(< r)$ within

**Figure 2.** TBW

spherical radius r . The calculation of g_{bar} requires the enclosed baryonic mass $M_{\text{bar}}(< r)$ of the galaxies, which consist of both stars and gas. We discuss our construction of $M_{\text{bar}}(< r)$ in Sect. 4.1.

The calculation of g_{obs} requires the enclosed observed mass $M_{\text{obs}}(< r)$ of the galaxy sample, which we obtain through the conversion of our observed ESD profile $\Delta\Sigma(R)$. To make sure this conversion is robust, we compare two different methods: a simple analytical method which assumes that DM haloes can be roughly approximated with a Singular Isothermal Sphere density model (Sect. 4.2), and an elaborate numerical approach which fits a piece-wise power law to the stacked ESD profile (Sect. 4.3) without any assumption on the averaged halo shape except for spherical symmetry. We validate both methods using mock surface density maps from the BAHAMAS simulation (Sect. 4.4).

4.1 Baryonic mass of the galaxies

is confined within our measurement radius ($R > 30$ kpc). This allows us to approximate $M_{\text{bar}}(< r)$ with the total baryonic mass of the galaxy M_{bar} , such that:

4.2 Singular Isothermal Sphere approximation

We start out from our ESD profile measurement, which consists of the value $\Delta\Sigma(R)$ measured in a set of R -bins. At our measurement radii ($R > 30 h^{-1}\text{kpc}$) the ESD is dominated by the DM halo. We can therefore adopt the simple assumption that our observed density profile $\rho_{\text{obs}}(r)$ is roughly described by a Singular Isothermal Sphere (SIS) model:

$$\rho_{\text{SIS}}(r) = \frac{\sigma^2}{2G\pi r^2}. \quad (8)$$

The SIS is generally considered to be the simplest parametrization of the spatial distribution of matter in an astronomical system (such as galaxies, clusters, etc.). It assumes that the dominant constituent particles (in our case DM) behave as an ideal gas that is confined by their combined spherically symmetric gravitational potential, where σ is the total velocity dispersion of the particles. Despite its

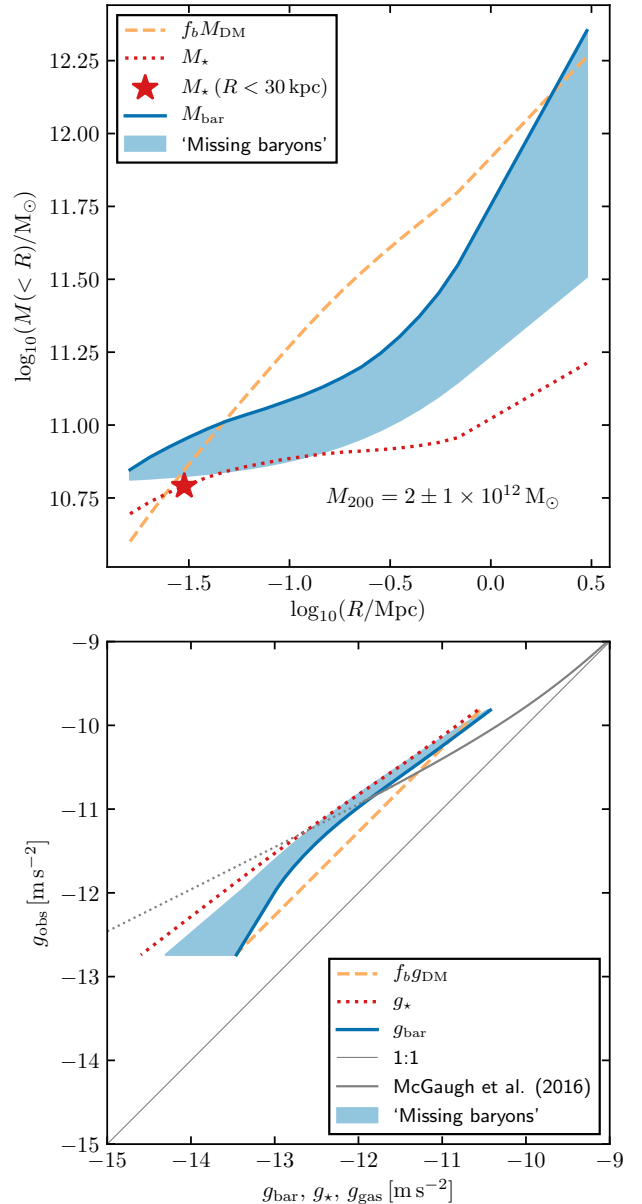


Figure 3. Mockup. Region 1-3 Mpc is extrapolated to give an idea, need to re-make once we get next batch of BAHAMAS data. *Upper panel:* Cumulative mass profiles of stars (dotted red) and baryons (solid blue) for BAHAMAS galaxies with $1 < M_{200}/10^{12} h^{-2} M_{\odot} < 3$. The star marker indicates the stellar mass within a 30 kpc aperture, indicative of what is typically regarded as the stellar mass of a galaxy. The blue shaded band shows an estimate based on fig. 7 of ? of the baryonic mass which would be ‘missing’ in even a multi-wavelength survey. In the inner galaxy only a small fraction of the baryons are missing, but in the outer galaxy the majority are missing. The yellow dashed line shows the expected baryonic mass profile if the baryon density is everywhere equal to a fixed fraction $f_b = \Omega_b/\Omega_m$ of the local dark matter density. At large enough radii ($\gtrsim 2$ Mpc), the baryon-to-DM ratio converges to the cosmic average. *Lower panel:* As in upper panel, but in acceleration space. The cosmic baryon fraction provides a robust upper limit on g_{bar} at low accelerations.

simple form, the ESD derived from the SIS profile:

$$\Delta\Sigma_{\text{SIS}}(R) = \frac{\sigma}{2GR}, \quad (9)$$

is generally able to describe WL measurements around galaxies and clusters (references). The SIS profile is therefore ideally suited to model the total enclosed mass distribution of our lenses, which can then be derived as follows:

$$M_{\text{SIS}}(< r) = 4\pi \int_0^r \rho_{\text{SIS}}(r') r'^2 dr' = \frac{2\sigma^2 r}{G}. \quad (10)$$

Now, for each measured value of $\Delta\Sigma_{\text{obs}}$ at its projected radius R , we assume that the entire density profile is described by a SIS with σ normalized such that $\Delta\Sigma_{\text{SIS}}(R)$ goes through $\Delta\Sigma_{\text{obs}}$. We also assume that the considered lens is flat, in order to approximate the spherical distance r with the measured transverse distance R . Using these assumptions, we can combine Eq. 9 and 10 to compute the observed enclosed mass distribution corresponding to that measurement:

$$M_{\text{obs}} = \frac{2(2GR\Delta\Sigma)r}{G} = 4\Delta\Sigma r^2. \quad (11)$$

Through Eq. 7, this results in a very simple expression for the observed gravitational acceleration:

$$g_{\text{obs}} = \frac{G(4\Delta\Sigma r^2)}{r^2} = 4G\Delta\Sigma, \quad (12)$$

computed at each point along the ESD profile.

4.3 Piece-wise power law density profile

We can instead assume a more self-consistent form for the volume density profile and parametrize it as a piece-wise power law constrained to be continuous. This comes at the cost of needing to invert the non-linear function $\Delta\Sigma(\rho)$, which we achieve via an iterative method. We choose to parametrize $\rho(r)$ in terms of N pairs of values (r_n, ρ_n) such that the slope a_n and normalization b_n of the power law profile segments are:

$$\log \rho = a_n \log(r) + b_n \quad (13)$$

$$a_n = \frac{\log(\rho_{n+1}) - \log(\rho_n)}{\log(r_{n+1}) - \log(r_n)} \quad (14)$$

$$b_n = \log(\rho_n) - a_n \log(r_n) \quad (15)$$

$$(a_n, b_n) = \begin{cases} (a_0, b_0) & \text{if } r < r_0 \\ (a_n, b_n) & \text{if } r_n \leq r < r_{n+1} \\ (a_{N-1}, b_{N-1}) & \text{if } r \geq r_N \end{cases} \quad (16)$$

(Throughout, \log denotes the natural logarithm.) We provide an expression for the discrete excess surface density profile in terms of the volume density profile, i.e. the function to be inverted, in Appendix A.

In order to invert $\Delta\Sigma_m(\rho_n)$, we take as constant the values $\{R_m\}$, $\{\Delta\Sigma_m\}_{\text{obs}}$ and $\{r_n\}$. We then propose an initial guess $\{\rho_n\}$ which we perturb iteratively, calculating the corresponding $\{\Delta\Sigma_m\}$ at each iteration and comparing with $\{\Delta\Sigma_m\}_{\text{obs}}$ via the likelihood function:

$$\log \mathcal{L} \propto -\frac{1}{2}(\Delta\Sigma_{\text{obs}} - \Delta\Sigma)^T \Sigma^{-1} (\Delta\Sigma_{\text{obs}} - \Delta\Sigma) \quad (17)$$

Note that Σ is the covariance matrix for the $\Delta\Sigma_{\text{obs}}$, not to be confused with the surface density. We use the package

EMCEE (Foreman-Mackey et al. 2013) to estimate the posterior probability distribution of $\{\rho_n\}$, and subsequently of the corresponding $\{g_{\text{obs},n}\}$ via integration of the volume density profile.

4.4 Testing the RAR conversion with BAHAMAS

5 THEORETICAL PREDICTIONS

5.1 Modified Newtonian Dynamics

With his theory of Modified Newtonian Dynamics (MOND), Milgrom (1983) postulated that the ‘missing mass problem’ in galaxies is not caused by an undiscovered fundamental particle, but that instead our current gravitational theory should be revised. MOND’s basic premise is that one can adjust Newton’s second law of motion ($F = ma$) by inserting a general function $\mu(a/a_0)$, which only comes into play when the acceleration a of a test mass m is much smaller than a critical acceleration a_0 . The goal of this function is to facilitate the discovered flat rotation curves in the outskirts of galaxies, while still reproducing the Newtonian behaviour of the inner disk. In short, the force F becomes:

$$F(a) = m \mu\left(\frac{a}{a_0}\right) a, \quad \mu(x \gg 1) \approx 1, \mu(x \ll 1) \approx x. \quad (18)$$

This implies that $a \gg a_0$ represents the Newtonian regime where $F_N = m a_N$ as expected, while $a \ll a_0$ represents the ‘deep-MOND’ regime where $F_{\text{dm}} = m a_{\text{dm}}^2/a_0$. In a circular orbit, this is reflected in the deep-MOND gravitational acceleration $g_{\text{dm}} \equiv a_{\text{dm}}$ as follows:

$$F_{\text{dm}} = m \frac{a_{\text{dm}}^2}{a_0} = \frac{G M m}{r^2} \rightarrow g_{\text{dm}} = \sqrt{a_0 \frac{GM}{r^2}}. \quad (19)$$

This can be written in terms of the expected baryonic acceleration $g_{\text{bar}} = GM/r^2$ as follows:

$$g_{\text{dm}}(g_{\text{bar}}) = \sqrt{a_0 g_{\text{bar}}}, \quad (20)$$

which demonstrates that MOND predicts a very simple relation for the RAR: $g_{\text{obs}} = g_{\text{bar}}$ in the Newtonian regime ($g_{\text{obs}} \gg a_0$), and following Eq. 19 in the deep-MOND regime ($g_{\text{obs}} \ll a_0$). However, since $\mu(a/a_0)$ (also known as the ‘interpolating function’) is not specified by Milgrom (1983), there is no specific constraint on the behaviour of this relation in between the two regimes. In the work of Milgrom & Sanders (2008), several families of interpolation functions are discussed. Selecting the third family (given by their Eq. 13) with constant parameter $\alpha = 1/2$, provides the function that M16 later used to fit to their measurement of the RAR using rotation curves 153 galaxies. This relation can be written as:

$$g_{\text{obs}} = \frac{g_{\text{bar}}}{1 - e^{-\sqrt{g_{\text{bar}}/a_0}}}. \quad (21)$$

where $a_0 \equiv g_{\text{f}}$ corresponds to the fitting parameter constrained by M16 to be $g_{\text{f}} = 1.20 \pm 26 \times 10^{-10} \text{ m/s}^2$. Since Eq. 21 (equal to Eq. 4 in M16) is also considered a viable version of the MOND interpolation function by Milgrom & Sanders (2008), we will consider it the baseline prediction of MOND in this work. As the baseline value of a_0 , we will likewise use the value of g_{f} measured by M16, since it exactly corresponds to the value of $a_0 = 1.2 \times 10^{-10} \text{ m/s}^2$ considered canonical in MOND since its first measurement by Begeman et al. (1991), using the rotation curves of 10 galaxies.

5.2 Emergent Gravity

The work of Verlinde (2016) (V16 hereafter), which is embedded in the framework of string theory and holography, shares the view that the missing mass problem is to be solved through a revision of our current gravitational theory. Building on the ideas of Jacobson (1995, 2016); Padmanabhan (2010); Faulkner et al. (2014) and his own previous work (Verlinde 2011), V16 abandons the notion of gravity as a fundamental force. Instead, it emerges from an underlying microscopic description of space-time, in which the notion of gravity has no a-priori meaning.

The aforementioned earlier works have shown that constructing a theory EG in a static ('anti-de Sitter') universe allows for the re-derivation Einstein's laws of GR. A distinguishing feature of V16 is that it attempts to describe an expanding ('de Sitter') universe, which is filled with a DE component. This results in a new volume law for gravitational entropy caused by DE, in addition to the area law normally used to retrieve Einsteinian gravity. According to V16, energy that is concentrated in the form of a baryonic mass distribution causes an elastic response in the entropy of the surrounding DE. This results in an additional gravitational component at scales set by the 'Hubble acceleration scale' $a_0 = cH_0$. Here c is the speed of light, and H_0 is the current Hubble constant which measures the Universe's expansion velocity.

Because this extra gravitational component is predicted to explain the effects usually attributed to DM, it is often expressed as an *apparent* dark matter (ADM) distribution:

$$M_D^2(r) = \frac{cH_0 r^2}{6G} \frac{d(M_b(r)r)}{dr}. \quad (22)$$

Thus the ADM distribution is completely defined by the baryonic mass distribution $M_b(r)$ as a function of the spherical radius r , and a set of known physical constants.

Since we measure the ESD profiles of galaxies at projected radial distances $R > 30 h_{70}^{-1} \text{Mpc}$, we can assume that their baryonic component is enclosed within the minimal measurement radius (see also Brouwer et al. 2017). This is equivalent to describing the galaxy as a point mass M_b , which allows us to simplify Eq. 22 to:

$$M_D(r) = \sqrt{\frac{cH_0 M_b}{6G}} r. \quad (23)$$

Now the total enclosed mass, $M_{EG}(r) = M_b + M_D(r)$, can be used to calculate the predicted gravitational acceleration $g_{EG}(r)$ as follows:

$$g_{EG}(r) = \frac{GM_{EG}(r)}{r^2} = \frac{GM_b}{r^2} + \sqrt{\frac{cH_0}{6}} \frac{\sqrt{GM_b}}{r}. \quad (24)$$

In terms of the expected baryonic acceleration $g_{\text{bar}}(r) = GM_b/r^2$, this simplifies even further to:

$$g_{EG}(g_{\text{bar}}) = g_{\text{bar}} + \sqrt{\frac{cH_0}{6}} \sqrt{g_{\text{bar}}}. \quad (25)$$

Note that Eq. 22 is only a macroscopic approximation of the underlying microscopic phenomena described at the start of this section, and is thus only valid for static, spherically symmetric and isolated baryonic mass distributions. For this reason, we select only the most isolated galaxies from our sample (see Sect. 3.2), such that our WL measurements are not influenced by neighbouring galaxies. In addition, cosmological evolution of the H_0 parameter is not

yet implemented in the theory, restricting its validity to galaxies with relatively low redshifts. However, we calculate that at our mean lens redshift ($\langle z \rangle \sim 0.2$) using an evolving $H(z)$ would result in only a 5% difference in our ESD measurements, based on the background cosmology used in this work.

In order to test V16 using the standard WL methodology, we need to assume that the deflection of photons by a gravitational potential in this alternative theory corresponds to that in GR. This assumption is justified because, in EG's original (anti-de Sitter) form, Einstein's laws emerge from its underlying description of space-time. The additional gravitational force described by ADM does not affect this underlying theory, which is an effective description of GR. Therefore, we assume that the gravitational potential of an ADM distribution produces the same lensing shear as an equivalent distribution of actual matter.

5.3 Analytical CDM model

To help guide an intuitive interpretation of the lensing RAR within the framework of the Λ CDM theory, we make use of the simple model of N17 which combines a basic model of galactic structure and scaling relations to predict the RAR. We refer to N17 for a full description, but give a summary here. A galaxy of a given stellar (or baryonic – there is no distinction in this model) mass occupies a dark matter halo of a mass fixed by the abundance matching relation of Behroozi et al. (2013). The dark halo concentration is fixed to the cosmological mean for haloes of that mass (Ludlow et al. 2014). The baryonic disc follows an exponential surface density profile with a half-mass size fixed to $0.2 \times$ the scale radius of the dark halo (N17). The above is sufficient to specify the cumulative mass profile of both the baryonic and dark components of the model galaxy; calculating g_{obs} and g_{bar} is then straightforward.

6 RESULTS

Write when the results are ready. I still need:

- The K1000 lensing catalogues with ANNz redshifts and stellar masses.
- The results from the Bahamas simulation.

6.1 Isolated galaxies

7 DISCUSSION AND CONCLUSION

ACKNOWLEDGEMENTS

Write at the end.

REFERENCES

- Abazajian K. N., et al., 2009, *ApJS*, **182**, 543
 Arnouts S., Cristiani S., Moscardini L., Matarrese S., Lucchin F., Fontana A., Giallongo E., 1999, *MNRAS*, **310**, 540
 Bartelmann M., Schneider P., 2001, *Phys. Rep.*, **340**, 291
 Begeman K. G., Broeils A. H., Sanders R. H., 1991, *MNRAS*, **249**, 523

- Behroozi P. S., Marchesini D., Wechsler R. H., Muzzin A., Papovich C., Stefanon M., 2013, *ApJ*, **777**, L10
- Bell E. F., de Jong R. S., 2001, *ApJ*, **550**, 212
- Benítez N., 2000, *ApJ*, **536**, 571
- Bernstein G. M., Guhathakurta P., Raychaudhury S., Giovanelli R., Haynes M. P., Herter T., Vogt N. P., 1994, *AJ*, **107**, 1962
- Bertin E., Arnouts S., 1996, *A&AS*, **117**, 393
- Bertone G., Tait T. M. P., 2018, *Nature*, **562**, 51
- Bertone G., Hooper D., Silk J., 2005, *Phys. Rep.*, **405**, 279
- Bilicki M., et al., 2017, preprint, ([arXiv:1709.04205](https://arxiv.org/abs/1709.04205))
- Blake C., et al., 2011, *MNRAS*, **415**, 2892
- Bosma A., 1981, *AJ*, **86**, 1791
- Brouwer M. M., et al., 2016, *MNRAS*, **462**, 4451
- Brouwer M. M., et al., 2017, *MNRAS*, **466**, 2547
- Brouwer M. M., et al., 2018, *MNRAS*, **481**, 5189
- Bruzual G., Charlot S., 2003, *MNRAS*, **344**, 1000
- Capaccioli M., Schipani P., 2011, *The Messenger*, **146**, 2
- Carretero J., Castander F. J., Gaztañaga E., Crocce M., Fosalba P., 2015, *MNRAS*, **447**, 646
- Crocce M., Castander F. J., Gaztañaga E., Fosalba P., Carretero J., 2015, *MNRAS*, **453**, 1513
- Desmond H., 2017, *MNRAS*, **464**, 4160
- Driver S. P., et al., 2011, *MNRAS*, **413**, 971
- Dvornik A., et al., 2017, *MNRAS*, **468**, 3251
- Dvornik A., et al., 2018, preprint, ([arXiv:1802.00734](https://arxiv.org/abs/1802.00734))
- Edge A., Sutherland W., Kuijken K., Driver S., McMahon R., Eales S., Emerson J. P., 2013, *The Messenger*, **154**, 32
- Eisenstein D. J., et al., 2005, *ApJ*, **633**, 560
- Erben T., et al., 2013, *MNRAS*, **433**, 2545
- Faulkner T., Guica M., Hartman T., Myers R. C., Van Raamsdonk M., 2014, *Journal of High Energy Physics*, **3**, 51
- Fenech Conti I., Herbonnet R., Hoekstra H., Merten J., Miller L., Viola M., 2017, *MNRAS*, **467**, 1627
- Fischer P., et al., 2000, *AJ*, **120**, 1198
- Foreman-Mackey D., Hogg D. W., Lang D., Goodman J., 2013, *PASP*, **125**, 306
- Fosalba P., Gaztañaga E., Castander F. J., Manera M., 2008, *MNRAS*, **391**, 435
- Fosalba P., Gaztañaga E., Castander F. J., Crocce M., 2015a, *MNRAS*, **447**, 1319
- Fosalba P., Crocce M., Gaztañaga E., Castander F. J., 2015b, *MNRAS*, **448**, 2987
- Hildebrandt H., et al., 2012, *MNRAS*, **421**, 2355
- Hildebrandt H., et al., 2017, *MNRAS*, **465**, 1454
- Hinshaw G., et al., 2013, *The Astrophysical Journal Supplement Series*, **208**, 19
- Hoekstra H., Yee H. K. C., Gladders M. D., 2004, *ApJ*, **606**, 67
- Hoffmann K., Bel J., Gaztañaga E., Crocce M., Fosalba P., Castander F. J., 2015, *MNRAS*, **447**, 1724
- Ilbert O., et al., 2006, *A&A*, **457**, 841
- Ilbert O., et al., 2009, *ApJ*, **690**, 1236
- Jacobson T., 1995, *Physical Review Letters*, **75**, 1260
- Jacobson T., 2016, *Physical Review Letters*, **116**, 201101
- de Jong J. T. A., Verdoes Kleijn G. A., Kuijken K. H., Valentijn E. A., 2013, *Experimental Astronomy*, **35**, 25
- de Jong J. T. A., et al., 2017, *A&A*, **604**, A134
- Keller B. W., Wadsley J. W., 2017, *ApJ*, **835**, L17
- Kuijken K., 2008, *A&A*, **482**, 1053
- Kuijken K., 2011, *The Messenger*, **146**, 8
- Kuijken K., et al., 2015, *MNRAS*, **454**, 3500
- Kuijken K., et al., 2019, arXiv e-prints, p. [arXiv:1902.11265](https://arxiv.org/abs/1902.11265)
- Lelli F., McGaugh S. S., Schombert J. M., 2016, *AJ*, **152**, 157
- von der Linden A., et al., 2014, *MNRAS*, **439**, 2
- Liske J., et al., 2015, *MNRAS*, **452**, 2087
- Ludlow A. D., Navarro J. F., Angulo R. E., Boylan-Kolchin M., Springel V., Frenk C., White S. D. M., 2014, *MNRAS*, **441**, 378
- Ludlow A. D., et al., 2017, *Phys. Rev. Lett.*, **118**, 161103
- Mandelbaum R., 2015, in Cappellari M., Courteau S., eds, IAU Symposium Vol. 311, Galaxy Masses as Constraints of Formation Models. pp 86–95 ([arXiv:1410.0734](https://arxiv.org/abs/1410.0734))
- Mandelbaum R., Seljak U., Kauffmann G., Hirata C. M., Brinkmann J., 2006, *MNRAS*, **368**, 715
- McCarthy I. G., Schaye J., Bird S., Le Brun A. M. C., 2017, *MNRAS*, **465**, 2936
- McFarland J. P., Verdoes-Kleijn G., Sikkema G., Helmich E. M., Boxhoorn D. R., Valentijn E. A., 2013, *Experimental Astronomy*, **35**, 45
- McGaugh S. S., 2004, *ApJ*, **609**, 652
- McGaugh S. S., 2012, *AJ*, **143**, 40
- McGaugh S. S., Schombert J. M., Bothun G. D., de Blok W. J. G., 2000, *ApJ*, **533**, L99
- McGaugh S. S., Lelli F., Schombert J. M., 2016, *Physical Review Letters*, **117**, 201101
- Milgrom M., 1983, *ApJ*, **270**, 365
- Milgrom M., Sanders R. H., 2008, *ApJ*, **678**, 131
- Miller L., Kitching T. D., Heymans C., Heavens A. F., van Waerbeke L., 2007, *MNRAS*, **382**, 315
- Miller L., et al., 2013, *MNRAS*, **429**, 2858
- Navarro J. F., Benítez-Llambay A., Fattahi A., Frenk C. S., Ludlow A. D., Oman K. A., Schaller M., Theuns T., 2017, *MNRAS*, **471**, 1841
- Padmanabhan T., 2010, *Reports on Progress in Physics*, **73**, 046901
- Pierce M. J., Tully R. B., 1988, *ApJ*, **330**, 579
- Planck VI x., 2018, arXiv e-prints, p. [arXiv:1807.06209](https://arxiv.org/abs/1807.06209)
- Planck XVI x., 2014, *A&A*, **571**, A16
- Robotham A. S., et al., 2011, *MNRAS*, **416**, 2640
- Rubin V. C., 1983, *Scientific American*, **248**, 96
- Sadeh I., Abdalla F. B., Lahav O., 2016, *PASP*, **128**, 104502
- Sanders R. H., 1986, *MNRAS*, **223**, 539
- Sanders R. H., 1996, *ApJ*, **473**, 117
- Sanders R. H., Noordermeer E., 2007, *MNRAS*, **379**, 702
- Schneider P., Kochanek C. S., Wambsganss J., 2006, Gravitational Lensing: Strong, Weak and Micro. Saas-Fee Advanced Courses, Swiss Society for Astrophysics and Astronomy, Springer, Berlin, Heidelberg, <http://cds.cern.ch/record/1339023>
- Sifón C., et al., 2015, *MNRAS*, **454**, 3938
- Spergel D. N., et al., 2003, *ApJS*, **148**, 175
- Taylor E. N., et al., 2011, *MNRAS*, **418**, 1587
- Tully R. B., Fisher J. R., 1977, *A&A*, **54**, 661
- van Uitert E., et al., 2016, *MNRAS*, **459**, 3251
- Verlinde E., 2011, *Journal of High Energy Physics*, **4**, 29
- Verlinde E. P., 2016, preprint, ([arXiv:1611.02269](https://arxiv.org/abs/1611.02269))
- Viel M., Becker G. D., Bolton J. S., Haehnelt M. G., 2013, *Phys. Rev. D*, **88**, 043502
- Viola M., et al., 2015, *MNRAS*, **452**, 3529
- Wu X., Kroupa P., 2015, *MNRAS*, **446**, 330
- Zehavi I., et al., 2011, *ApJ*, **736**, 59
- Zwicky F., 1937, *ApJ*, **86**, 217

APPENDIX A: EXCESS SURFACE DENSITY PROFILE OF A PIECE-WISE POWER LAW VOLUME DENSITY PROFILE

The excess surface density profile is measured in a series of discrete radial bins with edges R_m . The representative value at the centre of the bin – here we define the bin centre as $\frac{1}{2}(R_m + R_{m+1})$, i.e. not the ‘logarithmic centre’ $\sqrt{R_m R_{m+1}}$, which ensures accuracy in the calculation of the mean enclosed surface density – is $\Delta\Sigma_m = \bar{\Sigma}_m - \Sigma_m$, where $\bar{\Sigma}_m$ is the mean surface density within $\frac{1}{2}(R_m + R_{m+1})$ and Σ_m is the surface density averaged over the interval $[R_m, R_{m+1})$. We give an expression for this discrete excess surface density profile in terms of the parametric form for $\rho(r)$ given in Eq. 16.

The mean enclosed surface density is:

$$\bar{\Sigma}_m = \frac{1}{\pi R_m R_{m+1}} \left[I_1(0, \sqrt{R_0 R_1}, \tilde{a}_0, \tilde{b}_0) + \sum_{k=0}^m I_1(\sqrt{R_m R_{m+1}}, \sqrt{R_{m+1} R_{m+2}}, \tilde{a}_m, \tilde{b}_m) \right] \quad (\text{A1})$$

$$\tilde{a}_m = \frac{\log(\Sigma_{m+1}) - \log(\Sigma_m)}{\frac{1}{2}(\log(R_{m+2}) - \log(R_m))} \quad (\text{A2})$$

$$\tilde{b}_m = \log(\Sigma_m) - \frac{1}{2}\tilde{a}_m \log(R_m R_{m+1}) \quad (\text{A3})$$

$$I_1(R_i, R_j, \tilde{a}, \tilde{b}) = \frac{2\pi e^{\tilde{b}}}{\tilde{a} + 2} (R_j^{a+2} - R_i^{a+2}) \quad (\text{A4})$$

and the local surface density is given by:

$$\Sigma_m = \sum_{n=0}^{N-1} \begin{cases} 0 & \text{if } r_{n+1} < R_m \\ \frac{4e^{b_n}}{R_{m+1}^2 - R_m^2} (-I_2(r_{n+1}, R_m, a_n)) & \text{if } r_n < R_m \text{ and } R_m \leq r_{n+1} < R_{m+1} \\ \frac{4e^{b_n}}{R_{m+1}^2 - R_m^2} (I_2(r_{n+1}, R_{m+1}, a_n) - I_2(r_{n+1}, R_m, a_n)) & \text{if } r_n < R_m \text{ and } r_{n+1} \geq R_{m+1} \\ \frac{4e^{b_n}}{R_{m+1}^2 - R_m^2} (I_2(r_{n+1}, r_n, a_n) - I_2(r_{n+1}, R_m, a_n) \\ \quad + I_2(r_n, R_m, a_n) + I_2(r_{n+1}, R_{m+1}, a_n) \\ \quad - I_2(r_{n+1}, r_n, a_n)) & \text{if } R_m \leq r_n < R_{m+1} \text{ and } r_n \geq R_{m+1} \\ \frac{4e^{b_n}}{R_{m+1}^2 - R_m^2} (I_2(r_{n+1}, R_{m+1}, a_n) - I_2(r_{n+1}, R_m, a_n) \\ \quad - I_2(r_n, R_{m+1}, a_n) + I_2(r_n, R_m, a_n)) & \text{if } r_n \geq R_{m+1} \\ \frac{4e^{b_n}}{R_{m+1}^2 - R_m^2} (I_2(r_{n+1}, r_n, a_n) - I_2(r_{n+1}, R_m, a_n) \\ \quad + I_2(r_n, R_m, a_n) - I_2(r_{n+1}, r_n, a_n)) & \text{if } r_n \geq R_m \text{ and } r_{n+1} < R_m \end{cases} \quad (\text{A5})$$

$$I_2(r, R, a) = \begin{cases} -\frac{1}{3}R^{a+3} \left(\frac{r^2}{R^2} - 1 \right)^{\frac{3}{2}} {}_2F_1 \left(\frac{3}{2}, -\frac{a}{2}; \frac{5}{2}; 1 - \frac{r^2}{R^2} \right) & \text{if } r \text{ is finite} \\ \frac{\sqrt{\pi}}{2} \frac{\Gamma(-\frac{a+1}{2})}{\Gamma(-\frac{a}{2})} \frac{R^{a+3}}{a+3} & \text{if } r = \infty \end{cases} \quad (\text{A6})$$

where ${}_2F_1(\cdot, \cdot; \cdot; \cdot)$ is the Gaussian hypergeometric function and $\Gamma(\cdot)$ is the Gamma function.

This paper has been typeset from a \LaTeX file prepared by the author.